



Nanoscale

**Angle-Resolved Polarimetry of Hybrid Perovskite Emission
for Photonic Technologies**

Journal:	<i>Nanoscale</i>
Manuscript ID	NR-COM-06-2022-003261.R2
Article Type:	Communication
Date Submitted by the Author:	27-Oct-2022
Complete List of Authors:	Dhami, Bibek; University of Alabama at Birmingham College of Arts and Sciences, Department of Physics Iyer, Vasudevan; Oak Ridge National Laboratory Pant, Aniket; University of Alabama at Birmingham College of Arts and Sciences, Department of Physics Tripathi, Ravi Prakash; University of Alabama at Birmingham College of Arts and Sciences, Department of Physics Taylor, Ethan; University of Alabama at Birmingham College of Arts and Sciences, Department of Physics Lawrie, Benjamin J.; Oak Ridge National Laboratory, Appavoo, Kannatassen; University of Alabama at Birmingham College of Arts and Sciences, Department of Physics

SCHOLARONE™
Manuscripts

ARTICLE

Angle-Resolved Polarimetry of Hybrid Perovskite Emission for Photonic Technologies

Bibek S. Dhami,^{†a} Vasudevan Iyer,^{†b} Aniket Pant,^{†a} Ravi P.N. Tripathi,^a Ethan J. Taylor,^a Benjamin J. Lawrie^{b,c} and Kannatassen Appavoo^{*a}

Received 00th January 20xx,
Accepted 00th January 20xx

DOI: 10.1039/x0xx00000x

Coupling between light and matter strongly depends on the polarization of the electromagnetic field and the nature of the excitations in a material. As hybrid perovskites emerge as a promising class of materials for light-based technologies such as LEDs, lasers, and photodetectors, it is critical to understand how their microstructure changes the intrinsic properties of the photon emission process. While the majority of optical studies have focused on the spectral content, quantum efficiency and lifetimes of emission in various hybrid perovskite thin films and nanostructures, few studies have investigated other properties of the emitted photons such as polarization and emission angle. Here, we use angle-resolved cathodoluminescence microscopy to access the full polarization state of photons emitted from large-grain hybrid perovskite films with spatial resolution well below the optical diffraction limit. Mapping these Stokes parameters as a function of the angle at which the photons are emitted from the thin film surface, we reveal the effect of a grain boundary on the degree of polarization and angle at which the photons are emitted. Such studies of angle- and polarization-resolved emission at the single grain level are necessary for future development of perovskite-based flat optics, where effects of grain boundaries and interfaces need to be mitigated.

Introduction

Hybrid organic-inorganic perovskites, referred to herein as hybrid perovskites, have emerged as a promising class of materials for various solution-processed thin-film technologies such as solar-to-energy conversion¹⁻⁵, sensing and telecommunications⁶⁻⁸. With absorption and emission signatures that can be easily tuned from the visible to the near-IR by composition or doping⁸⁻¹⁰, this class of materials provides a playground for fundamental studies of a wide range of light-matter interactions under equilibrium (solar-like) and non-equilibrium (laser excitation) conditions. Although perovskite crystals have been studied for decades due to the exotic physics that arise from strong electron-correlation effects^{11, 12}, only recently was the organic-inorganic system stable enough to be considered for technological applications^{11, 12}. This improvement in crystallinity and the resilience of hybrid perovskites to adverse stimuli like humidity has resulted in ground-breaking power-conversion efficiencies exceeding 25% in single-junction photovoltaic devices^{13, 14}. Benefiting from recent progress in photovoltaic device engineering, other device applications^{2, 15-18} have been realized such as low-

threshold nanolasers^{8, 19}, radiation detectors⁷ and colour-filters⁶.

As hybrid perovskites find more applications in “flat” photonic technologies with critical dimensions at the nanoscale²⁰⁻²³ (e.g., light-emitting metasurfaces^{24, 25} and exciton-polariton microcavities^{26, 27}), it is clear that understanding the role of microstructures²⁸⁻³⁰, grain boundaries³¹⁻³⁶, grain junctions³⁷ and interfacial crystal heterogeneities³⁸⁻⁴⁰ will help to enhance their overall device efficiency. Moreover, for specialized detectors and emitters which require certain polarizing states and controlled angular emission profiles, it becomes critical to know the extent to which grain boundaries and interfaces randomize emission characteristics. In regards to characterizing the structural and morphological properties of hybrid perovskites, electron-beam spectroscopy techniques have been instrumental in providing insights with resolution below the diffraction limit⁴¹⁻⁴⁵. For example, transmission electron microscopy (TEM) coupled with electron energy-loss spectroscopy (EELS) or energy-dispersive X-ray spectroscopy (EDX) has been employed to provide insights into the crystallization process, grain orientations with respect to the substrates, and ion migration towards boundaries⁴³. Furthermore, electron backscatter diffraction (EBSD) measurements can probe crystallographic information and provide insights into the distribution of actual grain sizes created by various fabrication techniques. EBSD has also been used to probe the influence of grain-orientation heterogeneity (sub-grain boundaries and intra-grain misorientation) on local strain³⁸ and non-radiative recombination pathways³⁹ that ultimately determine the emission efficiency. Recently, by

^a Department of Physics, University of Alabama at Birmingham, AL 35205, USA

^b Centre for Nanophase Materials Science, Oak Ridge National Laboratory, TN, 37831, USA.

^c Materials Science and Technology Division, Oak Ridge National Laboratory, TN, 37831, USA.

[†] These authors contributed equally to this work.

Electronic Supplementary Information (ESI) available: [details of any supplementary information available should be included here]. See DOI: 10.1039/x0xx00000x

probing the crystallinity of hybrid perovskites at grain boundaries, EBSD has revealed the presence of amorphous grain boundaries that give rise to brighter emission as a consequence of longer carrier lifetimes³².

Recently, cathodoluminescence (CL) microscopy has emerged as a powerful tool to probe structure-function relationships of hybrid perovskites at the nanoscale^{41, 46-49}. CL has been used to describe how fine tuning of materials properties in halide perovskites can increase device efficiency and improve long-term stability. Additionally, in the field of nanophotonics, CL microscopy has been used to map nanoscale electromagnetic modes in plasmonic and all-dielectric metamaterial systems^{41, 50-52}. In more refined measurements, CL microscopy was used to probe other physical processes such as Purcell enhancement using plasmonics⁵³⁻⁵⁷, dispersion of quasiparticles such as surface plasmon polaritons^{58, 59} and collective Bloch modes in photonic crystals⁶⁰⁻⁶³.

In this work, we adapt a recently developed technique in cathodoluminescence spectroscopy to access the full polarization state of emission from a large-grain hybrid perovskite thin film and highlight the effect that a single boundary has on the polarization and angular profile of the emitted photons. We use a focused energetic electron beam as a broadband excitation source to interrogate nanoscale regions of interest. When the excited electrons and holes recombine, this results in emission. By tuning the electron-beam energy (across 1 – 30 keV), we can explore excited state energetics with both depth resolution in addition to the nanoscale lateral resolution provided by the converged electron beam. Thanks to this high degree of spatial resolution, typically few tens of nanometres, we can efficiently excite and probe emission with a relatively low background signal, allowing us to pinpoint the effects of grain boundaries and interfaces on emission properties. Similar to dark-field techniques, the emission generated from this excited region dominates the Fourier image, allowing us to determine the full angle-resolved polarization state of light emitted from these films. Encoded in the polarization of the emitted photons are details of the perovskite photophysics, including the local orientation of emission centres and symmetry-breaking structural changes in the film under investigation. To completely describe the polarization state of the light emission from our hybrid perovskite, we use the Mueller matrix formalism to determine the Stokes parameters of the emitted photons at the sample plane. We find that the emission intensity of the unpolarized light is strongly modulated by the presence of grain boundaries, though the angular emission profile is largely unchanged by grain boundaries. However, we show a strong angular dependence for polarized CL at the boundary of two grains, highlighting the complex emission mechanisms that occur at the nanoscale and suggesting that polarizing-dependent devices will benefit greatly from large-grain thin films, in addition the often-stated longer radiative recombination lifetimes.

Cathodoluminescence Microscopy

To access full polarization information in cathodoluminescence spectroscopy, we employ a technique pioneered by the Polman and Koenderink groups, originally based on polarization analysis in optical microscopes⁶⁴. An electron beam with energy between 1 – 30 keV excites the sample in an environmental scanning electron microscope. An aluminium parabolic mirror collects the CL emission from the sample and projects the emission on a two-dimensional 1024 × 256-pixel charge-coupled device (CCD) array which measures the intensity profile of the incoming emission beam. The distribution of the wavevectors in CL emission is then retrieved from the CCD image as each emission angle corresponds uniquely to a pixel on the CCD. As shown in Figure 1, the emitted photons can be analysed using different modalities including hyperspectral, polarized and angle-resolved imaging with a spatial resolution that is well below the diffraction limit. A rotating-plate polarimeter is included in the optical path that consists of a quarter-wave plate and a linear polarizer (Figure 1). The polarization of the light can be measured by varying the orientation of these optical elements. Importantly, the angle-dependent four Stokes parameters of the light can also be calculated, providing the most general representation of the polarization state of the cathodoluminescence^{64, 65}:

$$S_0 = |\hat{\epsilon}_1 \cdot \vec{E}|^2 + |\hat{\epsilon}_2 \cdot \vec{E}|^2 = I(0^\circ, 0) + I(90^\circ, 0)$$

$$S_1 = |\hat{\epsilon}_1 \cdot \vec{E}|^2 - |\hat{\epsilon}_2 \cdot \vec{E}|^2 = I(0^\circ, 0) - I(90^\circ, 0)$$

$$S_2 = 2 \Re \left[(\hat{\epsilon}_1 \cdot \vec{E})^* (\hat{\epsilon}_2 \cdot \vec{E}) \right] = I(45^\circ, 0) - I(135^\circ, 0)$$

$$S_3 = 2 \Im \left[(\hat{\epsilon}_1 \cdot \vec{E})^* (\hat{\epsilon}_2 \cdot \vec{E}) \right] = I\left(45^\circ, \frac{\pi}{2}\right) - I\left(135^\circ, \frac{\pi}{2}\right)$$

written in terms of general polarization basis sets that are orthogonal to each other. Here we choose $\hat{\epsilon}_1 = \hat{\epsilon}_\vartheta$ and $\hat{\epsilon}_2 = \hat{\epsilon}_\varphi$ for the detected emission from the source-sample frame. Thus, following detection of these raw-polarized images on our CCD (i.e., detector plane), the images are then projected onto the zenithal (also referred as radial, ϑ) and azimuthal (φ) space. To transform these to Stokes parameters in the sample plane, we use the appropriate Mueller matrix of the light collection system that accounts for the effect of the parabolic mirror on the polarization, where each element in this matrix is a function of the emission angle and wavelength. Included in this analysis are the effects of *s*- and *p*-polarized light based on the Fresnel coefficients of the mirror at the central frequency of the collection bandwidth.

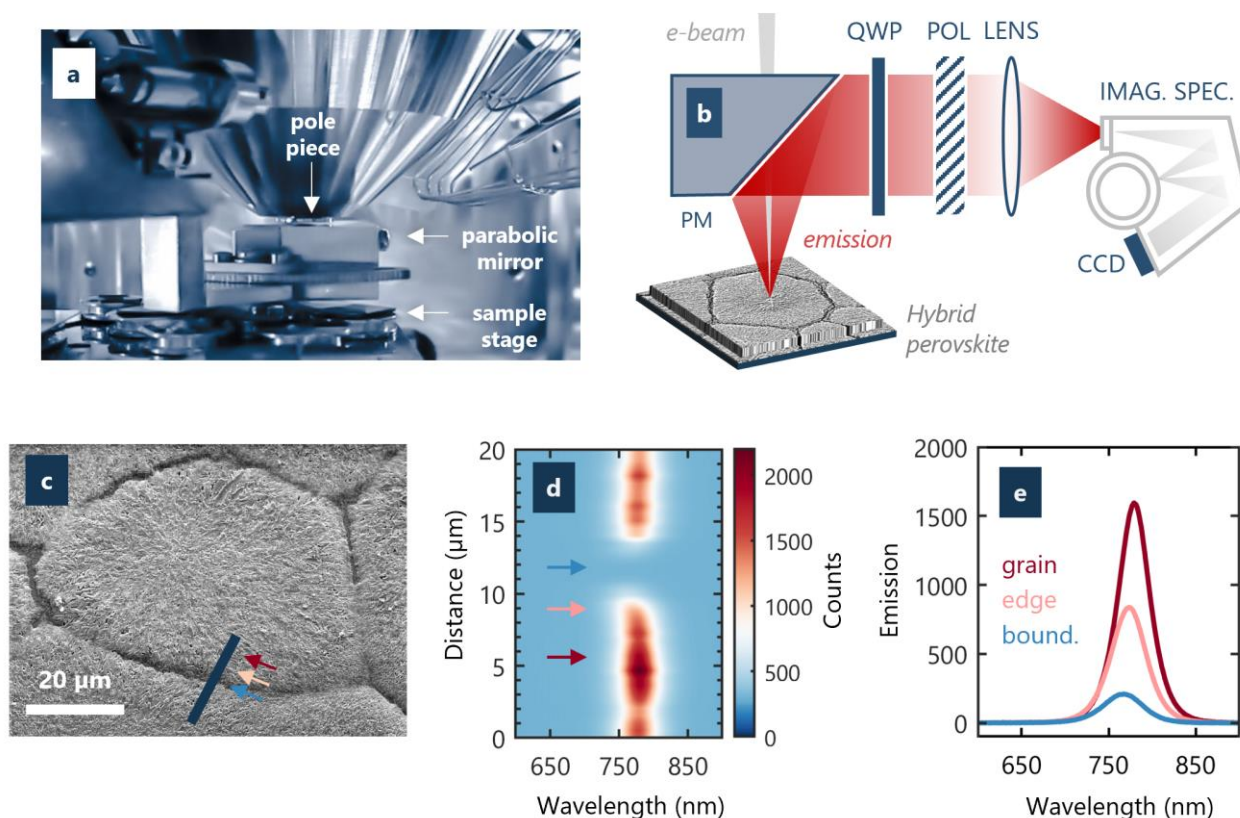


Figure 1: Overview of cathodoluminescence (CL) polarimetry characterization of hybrid perovskite at the single grain level. (a) Photograph of scanning electron microscope (SEM) chamber with CL polarimetry capabilities. (b) Schematics of angle-resolved CL polarimetry of large-grain hybrid perovskite where emitted photons are directed to the detector using an off-axis parabolic mirror, analysed using rotating-plate optical polarimeter components placed in the beam path. PM: Parabolic mirror; QWP: Quarter wave plate; POL: Polarizer; IMAG. SPEC.: Imaging Spectrometer; CCD: charged-coupled device. (c) Scanning electron micrograph of a representative grain of hybrid perovskite which was studied. Dark blue line represents a spatially selected linescan of 20 micrometres in length, here crossing the boundary of two grains. (d) CL spectrum as a function of scanned distance. Pseudo-colour plot of emission wavelength vs. spatial distance, with the suppressed axis representing intensity of the CL. (e) For the three arrows drawn in figure (c, d), typical spectra at the grain centre (red), edge (pink) and boundary (blue) are plotted. Note the non-negligible emission at the boundary caused by excitation near the two grain interfaces.

Cathodoluminescence Polarimetry on Hybrid Perovskites

To understand how the morphology of a grain and its boundaries modify the intensity and polarization properties of the emission process, we investigate a large-grain hybrid perovskite with maximum emission near its band edge ($\lambda \sim 760 \text{ nm}$). Fabrication and characterization of the hybrid perovskite, here prototypical methylammonium lead iodide ($\text{CH}_3\text{NH}_3\text{PbI}_3 = \text{MAPbI}_3$), are described in the *Methods* section and in references^{36,66}. Initially, we use spatially resolved CL spectroscopy by combining scanning electron microscopy with the detection of CL that is emitted from the sample (Figure 1c, d). We perform the CL mapping and polarimetry using a 5 kV, 110 pA electron beam. CL mapping was performed by collecting one spectrum for each pixel with an acquisition time of 100 ms to form a 256×256 -pixel image of a hybrid

perovskite domain (Figure 1c). These samples fabricated using solution-process techniques contain several defects and trap states that are mostly located at the grain boundaries. Several previous studies on MAPbI_3 perovskite have reported these defects including vacancies, interstitial defect, Frankel and Schottky defects⁶⁷⁻⁶⁹. A linescan through the SEM/CL map along a grain boundary shows the change in emission spectrum as a function of location of the electron-beam excitation on the hybrid perovskite (Figure 1d, e). As we excite and detect emission closer to the boundary of the hybrid perovskite grains, the intensity decreases and there is an apparent slight blue shift in the CL. The decrease in the emission intensity is caused by the limited amount of hybrid perovskite at the boundary, while the apparent blue shift in CL emission is attributed to the formation of intermediate phase of hybrid perovskite (Figure S1 and S2) that are more prone to formation near the boundary, as documented by Taylor et al. in hyperspectral mapping of hybrid perovskite at the single grain level⁷⁰. Similar blue shift has also been observed previously by Hentz et al.⁷¹ and Koasasih et al.⁷²

Because spatially resolving polarization state of CL require increased electron beam doses, an understanding of electron-beam-induced damage in MAPbI_3 is critical. We find that for large beam energy (> 10 kV) or current (> 2 nA), spectral changes over time were visible within the first 10 seconds of CL collection. CL peak broadening accompanied by a decrease in peak intensity most likely resulted from nonradiative decay pathways as defects were created by the electron beam. Furthermore, when nanoscale areas of the hybrid perovskite are exposed to the 10 kV or 20 kV electron beam for 10s of seconds, two new CL peaks emerge at higher photon energy. A CL peak at ~ 660 nm (1.88 eV) is attributed to intermediate phases that are formed during the perovskite decomposition and caused by electron-beam-induced heating. Hybrid perovskites are poor electrical and thermal conductors and such a focused beam (~ 5 nm) could conceivably create local heating effects. The CL peak at the highest photon energy of 525 nm (2.36 eV), corresponds to the presence of PbI_2 . The PbI_2 CL is stable over extended periods under exposure to the electron beam and is not reversible, unlike changes caused by an intense laser source⁷³. These observations are well aligned with the extensive work by Xiao et al.⁷⁴, where the authors conducted in situ studies of high-energy electron beam interaction with hybrid perovskites. Two damage mechanisms were proposed, including nanoscale local heating and ion displacement via the knock-on or Frenkel defect mechanism. Importantly for our studies, it is found that an irradiation power of $\sim 5 \times 10^{10}$ W/m² minimize damage to the hybrid perovskite. Therefore, for the remainder of this work, we excite the hybrid perovskite with electron beam having power that lies well below this threshold, in the $0.5 - 1 \times 10^{10}$ W/m² range.

Results and Discussions

Figure 2 illustrates the normalized angle-dependent, four Stokes parameters at the sample plane ($S_0, S_{1N}, S_{2N}, S_{3N}$) that have been calculated from the six polarization measurements described above — comparing between the two extreme cases in our film, i.e., emission collected from a grain centre (left panels) and emission collected at the boundary (right panels). The topmost panels correspond to the total intensity distribution, S_0 . To compare features in the polarization at all angles, all the panels are normalized with respect to S_0 . In these polar plots, the radial direction represents ϑ , the polar angle represents φ , and the color scheme represents the normalized emission intensity. In both S_0 cases, the semiconductor film of hybrid perovskite emits in a Lambertian distribution, a direct consequence of Snell's Law⁷⁵. This emission distribution with its characteristic cosine dependence on the zenithal angle is expected for semiconductors and dielectrics because they radiate incoherently in the material via spontaneous emission⁷⁶. Here, the effects of the boundary on the emission polarization are readily seen in the parameters S_{1N} and S_{2N} that are highly dependent on the emission angle, while for the grain centre, all emission pattern plots are fairly monotonic in nature, with little angular dependence²¹. The shaded region that broadens from

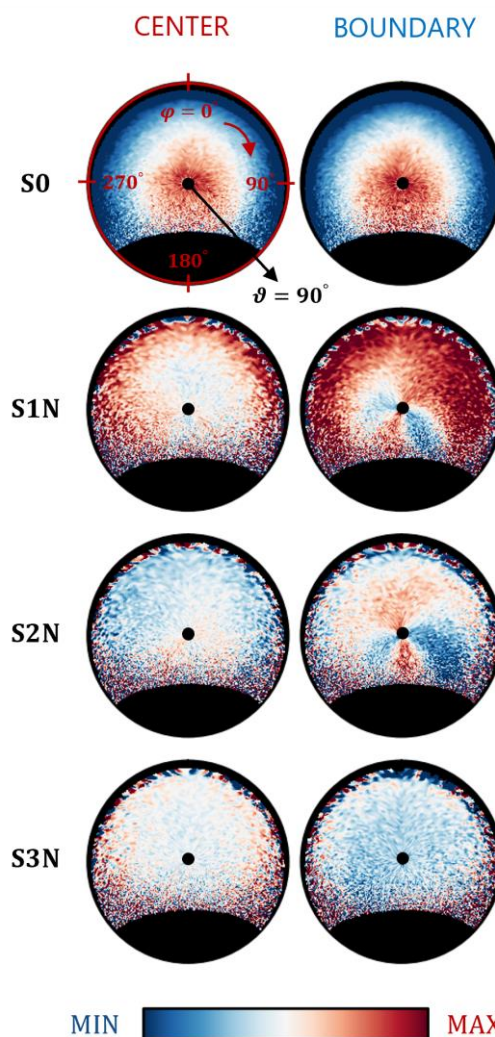


Figure 2: Stokes parameters of CL in hybrid perovskite. Angle-resolved Stokes parameters in the sample plane comparing CL from the grain centre (left column) and CL from the grain boundary (right column) mapped onto the polar coordinates (azimuthal angle φ and zenithal angle ϑ). The S_{1N}, S_{2N} and S_{3N} parameters have been normalized to their respective S_0 to easily compare between the overall polarization distribution. For example, strong linear polarization dependence (S_{1N} and S_{2N}) is visible for the grain boundary case.

$\varphi = 135^\circ$ to $\varphi = 225^\circ$ for $\vartheta > 40^\circ$ corresponds to an opening in the parabolic mirror where no emitted light is collected. Similarly, a small portion of the emission around $\vartheta = 0^\circ$ is not collected due to the hole in the mirror that allows the electron beam to pass from the SEM pole piece to the sample.

Having retrieved the Stokes parameters for the emission of our sample, we can now compute its electric field components. To know how maps of far-field emission are derived from local radiating sources, we reconstruct the spherical field vector amplitudes $|\hat{e}_\vartheta \cdot \vec{E}|$ and $|\hat{e}_\varphi \cdot \vec{E}|$ that correspond to the intrinsic parallel (p -) and perpendicular (s -) polarization basis set relevant to our system, with respect to the plane of incidence as defined by the propagation vector (\vec{k}).

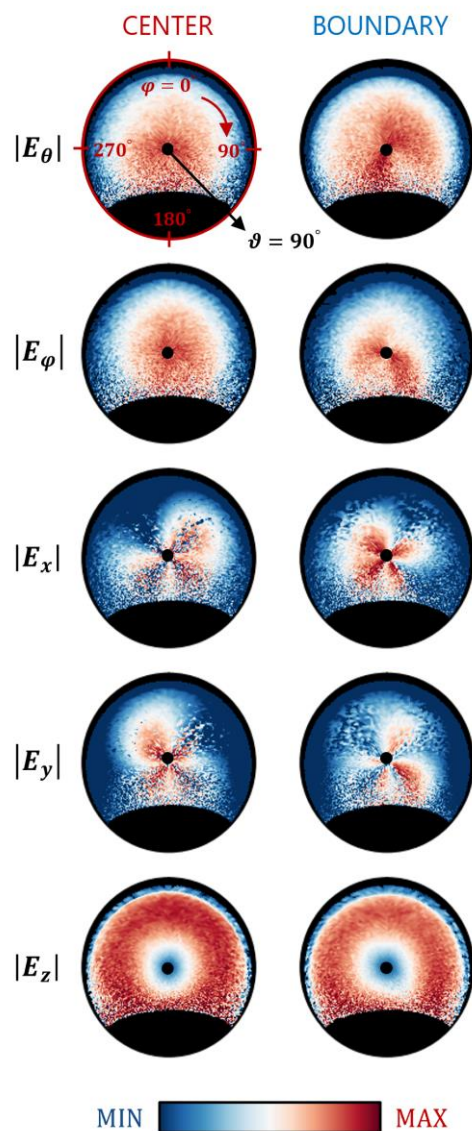


Figure 3: Retrieved electric field amplitude distributions. Angle-resolved spherical and Cartesian electric field amplitude distributions for CL from the grain centre (left column) and from the grain boundary (right column). Note that the amplitudes $|\vec{E}_\theta|$ and $|\vec{E}_\varphi|$ corresponds to the *s*- and *p*-polarization basis that map the far-field generated by a localized emission event and are the components that highlight differences in the overall emission as a function of angle.

The right panels of Figure 3 show that at the grain centre, the $|\vec{E}_\theta|$ and $|\vec{E}_\varphi|$ distributions are strong and azimuthally symmetric. This feature is expected since the filtered emission ($\lambda = 750 \pm 25 \text{ nm}$) originates from the incoherent spontaneous emission process within the bulk hybrid perovskite film. At the grain boundary, however, we see that the electric field amplitude is highly angle dependent. These results highlight the complex morphology of grain boundaries at the nanoscale and their role in modulating strongly the emission direction and polarization. These results are novel, complementing the well-studied changes in spectral content and intensity of the emitted photons that occur at grain

boundaries and junctions^{32, 39, 77}. Here, CL-enabled microscopy allows us to retrieve emission properties well below the diffraction limit and demonstrate the impact of a single grain boundary on the emission purity.

Furthermore, the polarization can also be disentangled in Cartesian space, i.e., using vector amplitudes $|\vec{E}_x|$, $|\vec{E}_y|$ and $|\vec{E}_z|$. Plotted this way, we see that emission in the sample plane has also a complex angular dependence, with a four-lobe pattern. However, in our specific case, such electric field decomposition in the sample plane provides little information between emission from the grain centre and its boundary. For these two selected regions of interest (centre or boundary), we see complimentary polarization in the $|\vec{E}_x|$ and $|\vec{E}_y|$ direction. Presumably, this demonstrates that $|\vec{E}_\theta|$ and $|\vec{E}_\varphi|$ decompositions provide more insights for characterizing the effect of interfaces in thin film semiconductors while $|\vec{E}_x|$ and $|\vec{E}_y|$ decompositions are more appropriate for plasmonic and metallic thin films. In other words, $|\vec{E}_\theta|$ and $|\vec{E}_\varphi|$ components are adequate probes for detecting in-plane symmetry breaking effects. Taking a look at the $|\vec{E}_z|$ component, we see a characteristic doughnut shape, corresponding to a decrease in that component as ϑ approaches zero. In other words, since the electric field is necessarily transverse to the propagation vector \vec{k} , $|\vec{E}_z|$ vanishes at near-normal angles. Furthermore, for the grain boundary case, we see an overall decrease in the magnitude of this component, accompanied by a narrower range of emission angle. Two potential factors for a decrease in emission are a reduction in local sources of emission at the boundary (i.e., increase in non-radiative decay channels), and emission from local dipoles that are deeper in the grain (but exposed thanks to the presence of the boundary). Both will result in greater scattering of the emission since the feature sizes of the interface are on the same order as the emission wavelength.

The degree of linear polarization (DOLP) and the degree of circular polarization (DOCP) can also be calculated from the measured Stokes parameters. These parameters are given by the ratio of polarization with respect to the total intensity and thus, DOLP is given by $\sqrt{(S_1^2 + S_2^2)}/S_0$ and DOCP is given by S_3/S_0 . Figure 4 highlights the difference in DOLP and DOCP between the centre and boundary of the grain. At the boundary, the symmetry breaking in the sample plane causes linear polarization to increase as ϑ approaches 90° . Moreover, for an in-plane angular range of φ ($0 - 90^\circ$), we see that there is also an increase in the DOLP, likely because the electron beam is not perfectly at the centre of the grain boundary. We note that for $\vartheta > 60^\circ$, the DOLP appears higher for the grain boundary case. A similar effect is seen for the DOCP, whereby the grain boundary exhibits a greater degree of circular polarization (negative in this case). For the case of the grain centre, the relatively flat morphology of the thin film results in a negligible DOCP as expected from the isotropic spontaneous emission process.

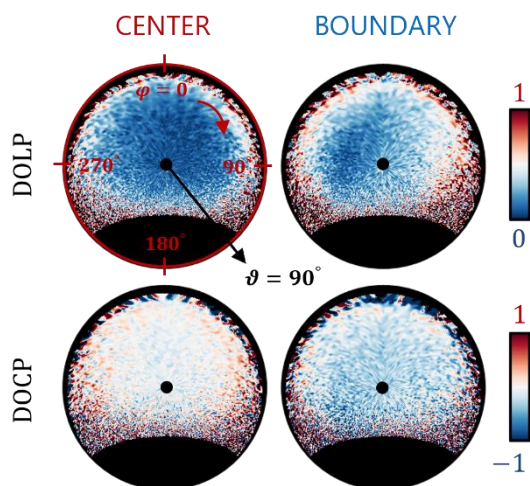


Figure 4: Comparison of degree of polarization in CL. Degree of linear polarization (DOLP) and degree of circular polarization (DOCP) between CL from grain centre (left column) and grain boundary (right column) as a function of angle. For the boundary case, DOLP shows an asymmetrical emission profile while the DOCP plot shows a slightly negative polarization dependence (blue).

In Figure 5, we visualized the directionality of emission by integrating the azimuthal component of the emission (φ ranging from $90^\circ - 270^\circ$, counter-clockwise) and plot the zenithal cross cuts for both the polarized ($S_0 \times DOP$) and unpolarized ($S_0 \times (1 - DOP)$) cases. We note that a narrow cone of light emitted perpendicular from the sample is not collected (i.e., θ near 0°) due the aperture geometry of the parabolic mirror with respect to the incoming electron beam and expects emission at those angles. The total angle-resolved CL is plotted in figure 5a, demonstrating that indeed emission from the hybrid perovskite is mostly unpolarized with a Lambertian-type profile; CL is reduced at the grain boundary either due to an increase in non-radiative decay channels or a decrease in local emission sources caused essentially by less hybrid perovskite material being present at the boundary. Furthermore, we see that polarized emission is lower than its unpolarized counterpart in both cases; it is about an order of magnitude less for the grain centre and about three times less for the grain boundary. Since we collect and analyse emission only from band-to-band recombination (near $\lambda = 760 \text{ nm}$) the emission inside the bulk thin film is incoherent, unpolarized and isotropic. Thus, the slight polarized emission for the grain centre data (red solid line) collected by our system is a result of the semiconductor-vacuum interface with large differences between the s - and p -Fresnel transmission coefficients. The angular distribution of this weak polarized emission is different from the unpolarized emission and agrees with Fresnel calculations, which display an increase of T_p vs. T_s as the outgoing angle increases, i.e., as ϑ approaches 90° . This angular emission profile is rather complex as it is attributed both to changes of polarization at the interface, and to other factors such as changes in the total internal reflection caused by the film morphologies which restrict emission beyond a certain angle. Furthermore, photon-recycling also play a role in modifying the radiative properties of hybrid perovskites^{20, 78},

and could redistribute the angular emission profile within the spectral content studied. Because hybrid perovskites have strong bandedge CL and the collected emission was filtered, coherent transition radiation plays little role in the angular profile of weak polarized emission. A similar conclusion was reached for GaAs^{64, 76}. An important observation from Figure 5 is that the weak polarized emission from the grain boundary is peaked both at $\vartheta = 45^\circ$ and unexpectedly at $\vartheta = 0^\circ$. We attribute this angle-dependent emission profile to the tow vertical surfaces of the boundary (i.e., perpendicular to the substrate) that polarises the emission in a similar fashion as the

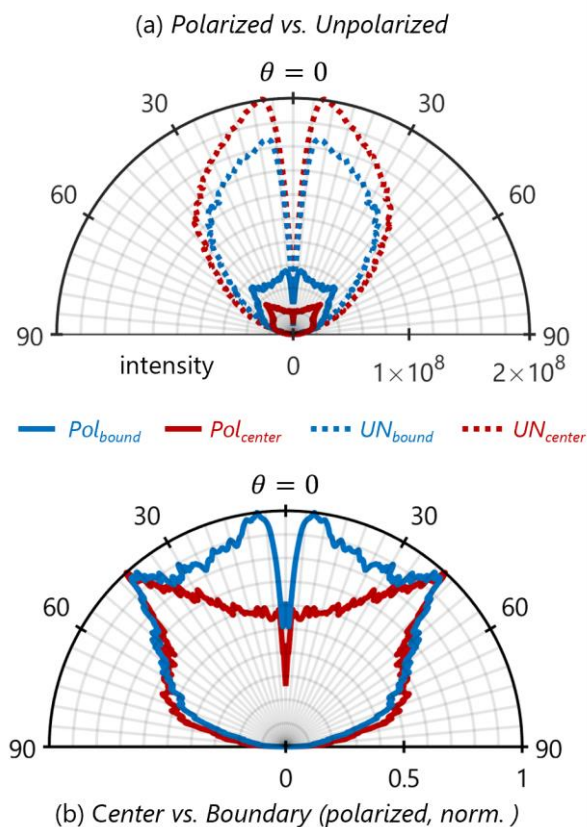


Figure 5: Polarized and unpolarized zenithal emission from hybrid perovskite. (a) Zenithal cross cuts comparing polarized (line) and unpolarized (dash) emission counts from the grain centre (red) and grain boundary (blue) at $\lambda = 750 \text{ nm}$. (b) Normalized zenithal cross cuts to highlight effect of the boundary on the polarized emission, where we scale the angular distributions by the overall polarized emission intensity. The data has been obtained by averaging over the azimuthal range $\varphi = 90^\circ - 270^\circ$, counter-clockwise to improve signal-to-noise ratio.

grain centre. Consequently, the additional emission at the boundary results in this peculiar angular emission profile (Figure 5b, blue) and is roughly twice the amount of polarised light from a single surface (Figure 5a). A careful look between the red and blue lines in Figure 5a shows that the polarized emission at the boundary is indeed higher than the emission intensity at the grain centre.

Conclusions

Our data show that precise electron-beam excitation and polarimetry analysis of the CL provides quantitative information about the emission in large-grain hybrid perovskite thin films. We use this novel technique to map the vectorial electromagnetic emission properties of this nanostructured thin film, and importantly separate polarized and unpolarized emission, which can also be used to determine different mechanisms that contribute to emission processes in this technologically relevant material. Thanks to the high resolution of the electron beam excitation, the wave-vector resolved polarization properties of locally excited emissive events can be extracted with a spatial resolution below the diffraction limit. Moreover, we also demonstrate how structural asymmetry translates into changes in linear and circular polarized emitted light. This demonstration of nanoscale characterization highlights the advantages of SEM-CL to locally study material anisotropy and optical activity near grain boundaries. Importantly, our study highlights another advantage of using large-grain over small-grain thin films of hybrid perovskite beyond the radiative lifetime and quantum efficiency reasons — better emission purity for photonics devices.

Methods

Fabrication of hybrid perovskite: Hybrid perovskite thin films were prepared using hot-casting technique⁶⁶. The perovskite precursor solution is made by mixing **0.2 gram** methyl ammonium iodide ($\text{CH}_3\text{NH}_3\text{PbI}_3 = \text{MAPbI}_3$, Sigma Aldrich, **98 %**) and **0.578 gram** lead iodide (PbI_2 , Sigma Aldrich, **99 %**) in **1.0 ml** of anhydrous, N, N-Dimethyl formamide (**DMF**, Sigma Aldrich, **99 %**). The mixture solution was then heated at **120°C**. We used borosilicate microscopic glass slides as the substrate. The glass substrates are cleaned by isopropanol (Sigma Aldrich, **99 %**) using ultrasonication. We heated these cleaned substrates to **300°C**. We then spin-coated the preheated perovskite-precursor solution onto preheated substrate at **5000 rpm** for **5 seconds** and quickly transferred the substrate on the hotplate maintained at **300°C** for **2 seconds**. Subsequently, we obtained thin film of hybrid perovskite with large grain features. This fabrication process was performed inside a N₂ filled glovebox.

Cathodoluminescence microscopy: CL microscopy was performed in a FEI Quattro environmental scanning electron microscope with a Delmic Sparc cathodoluminescence system. A beam energy of **5 keV** and beam current of **110 pA** were used. The sample chamber was maintained at a pressure of 2×10^{-3} Pa. CL spectra were acquired with a high numerical aperture (0.9) parabolic mirror and sent to an Andor Kymera 193i spectrometer equipped with a **150 line/mm** grating and an Andor Newton CCD camera. For the angle-resolved measurements, the sample was exposed for **500 ms** at each polarizer orientation, resulting in a total exposure of **3 seconds**

per acquisition. The Fourier plane of the image is obtained by using an appropriate lens and replacing the grating in the spectrometer with a mirror. The exposure time for standard spectrum imaging was **100 ms** per pixel.

Author Contributions

BSD and RPNT fabricated the hybrid perovskite sample. VI conducted the CL microscopy. BSD, AP, EJT and KA analysed the data. All authors contributed to writing the manuscript. KA and BJL designed and oversaw the project.

Conflicts of interest

The authors declare no conflicts of interest.

Acknowledgements

Support for this project was provided by NASA EPSCoR RID (award number 80NSSC19M0051) and UAB start-up funds. Cathodoluminescence microscopy was supported by the Center for Nanophase Materials Sciences (CNMS), which is a US Department of Energy, Office of Science User Facility at Oak Ridge National Laboratory. BSD acknowledges financial support from the Alabama Graduate Research Scholars Program (GRSP) funded through the Alabama Commission for Higher Education and administered by the Alabama EPSCoR. AP was supported by the National Aeronautics and Space Administration (NASA), Alabama Space Grant Consortium, Research Experiences for Undergraduates (REU) at UAB. KA was partly supported by the Ralph E. Powe Junior Faculty Enhancement Award, from the Oak Ridge Associated Universities (ORAU).

References

1. M. M. Lee, J. Teuscher, T. Miyasaka, T. N. Murakami and H. J. Snaith, *Science*, 2012, **338**, 643-647.
2. J. Burschka, N. Pellet, S.-J. Moon, R. Humphry-Baker, P. Gao, M. K. Nazeeruddin and M. Graetzel, *Nature*, 2013, **499**, 316-+.
3. H. J. Snaith, *The Journal of Physical Chemistry Letters*, 2013, **4**, 3623-3630.
4. Z.-K. Tan, R. S. Moghaddam, M. L. Lai, P. Docampo, R. Higler, F. Deschler, M. Price, A. Sadhanala, L. M. Pazos, D. Credgington, F. Hanusch, T. Bein, H. J. Snaith and R. H. Friend, *Nat Nano*, 2014, **9**, 687-692.
5. S. D. Stranks and H. J. Snaith, *Nat Nano*, 2015, **10**, 391-402.
6. Q. Lin, A. Armin, P. L. Burn and P. Meredith, *Nat Photon*, 2015, **9**, 687-694.
7. S. Yakunin, M. Sytnyk, D. Kriegner, S. Shrestha, M. Richter, G. J. Matt, H. Azimi, C. J. Brabec, J. Stangl, M. V. Kovalenko and W. Heiss, *Nat Photon*, 2015, **9**, 444-449.
8. H. Zhu, Y. Fu, F. Meng, X. Wu, Z. Gong, Q. Ding, M. V. Gustafsson, M. T. Trinh, S. Jin and X. Y. Zhu, *Nat Mater*, 2015, **14**, 636-642.

9. S. A. Kulkarni, T. Baikie, P. P. Boix, N. Yantara, N. Mathews and S. Mhaisalkar, *Journal of Materials Chemistry A*, 2014, **2**, 9221-9225.
10. G. Xing, N. Mathews, S. S. Lim, N. Yantara, X. Liu, D. Sabba, M. Grätzel, S. Mhaisalkar and T. C. Sum, *Nat Mater*, 2014, **13**, 476-480.
11. A. Poglitsch and D. Weber, *The Journal of Chemical Physics*, 1987, **87**, 6373-6378.
12. D. B. Mitzi, C. A. Feild, W. T. A. Harrison and A. M. Guloy, *Nature*, 1994, **369**, 467-469.
13. J. Jeong, M. Kim, J. Seo, H. Lu, P. Ahlawat, A. Mishra, Y. Yang, M. A. Hope, F. T. Eickemeyer, M. Kim, Y. J. Yoon, I. W. Choi, B. P. Darwich, S. J. Choi, Y. Jo, J. H. Lee, B. Walker, S. M. Zakeeruddin, L. Emsley, U. Rothlisberger, A. Hagfeldt, D. S. Kim, M. Grätzel and J. Y. Kim, *Nature*, 2021, **592**, 381-385.
14. J. J. Yoo, G. Seo, M. R. Chua, T. G. Park, Y. Lu, F. Rotermund, Y.-K. Kim, C. S. Moon, N. J. Jeon, J.-P. Correa-Baena, V. Bulović, S. S. Shin, M. G. Bawendi and J. Seo, *Nature*, 2021, **590**, 587-593.
15. A. Abrusci, S. D. Stranks, P. Docampo, H.-L. Yip, A. K. Y. Jen and H. J. Snaith, *Nano Lett.*, 2013, **13**, 3124-3128.
16. J.-H. Im, I.-H. Jang, N. Pellet, M. Grätzel and N.-G. Park, *Nat Nano*, 2014, **advance online publication**.
17. G. Xing, N. Mathews, S. Sun, S. S. Lim, Y. M. Lam, M. Grätzel, S. Mhaisalkar and T. C. Sum, *Science*, 2013, **342**, 344-347.
18. W. Zhang, M. Saliba, S. D. Stranks, Y. Sun, X. Shi, U. Wiesner and H. J. Snaith, *Nano Lett.*, 2013, **13**, 4505-4510.
19. E. National Academies of Sciences and Medicine, *Testing at the Speed of Light: The State of U.S. Electronic Parts Space Radiation Testing Infrastructure*, The National Academies Press, Washington, DC, 2018.
20. J. Huang, Y. Yuan, Y. Shao and Y. Yan, *Nature Reviews Materials*, 2017, **2**, 17042.
21. S. A. Veldhuis, P. P. Boix, N. Yantara, M. Li, T. C. Sum, N. Mathews and S. G. Mhaisalkar, *Adv. Mater.*, 2016, **28**, 6804-6834.
22. S. Chen and G. Shi, *Adv. Mater.*, 2017, **29**, 1605448.
23. Q. Zhang, R. Su, W. Du, X. Liu, L. Zhao, S. T. Ha and Q. Xiong, *Small Methods*, 2017, **1**, 1700163.
24. S. Liu, A. Vaskin, S. Addamane, B. Leung, M.-C. Tsai, Y. Yang, P. P. Vabishchevich, G. A. Keeler, G. Wang, X. He, Y. Kim, N. F. Hartmann, H. Htoon, S. K. Doorn, M. Zilk, T. Pertsch, G. Balakrishnan, M. B. Sinclair, I. Staude and I. Brener, *Nano Lett.*, 2018, **18**, 6906-6914.
25. Y. Mohtashami, R. A. DeCrescent, L. K. Heki, P. P. Iyer, N. A. Butakov, M. S. Wong, A. Alhassan, W. J. Mitchell, S. Nakamura, S. P. DenBaars and J. A. Schuller, *Nature Communications*, 2021, **12**, 3591.
26. P. Bouteyre, H. S. Nguyen, J.-S. Lauret, G. Trippé-Allard, G. Delport, F. Lédée, H. Diab, A. Belarouci, C. Seassal, D. Garrot, F. Bretenaker and E. Deleporte, *ACS Photonics*, 2019, **6**, 1804-1811.
27. A. Fieramosca, L. Polimeno, V. Ardizzone, L. De Marco, M. Pugliese, V. Maiorano, M. De Giorgi, L. Dominici, G. Gigli, D. Gerace, D. Ballarini and D. Sanvitto, *Science Advances*, 2019, **5**, eaav9967.
28. D. W. de Quilettes, S. M. Vorpahl, S. D. Stranks, H. Nagaoka, G. Eperon, M. E. Ziffer, H. J. Snaith and D. S. Ginger, *Science*, 2015, **348**, 683-686.
29. G. Grancini, A. R. Srimath Kandada, J. M. Frost, A. J. Barker, M. De Bastiani, M. Gandini, S. Marras, G. Lanzani, A. Walsh and A. Petrozza, *Nature Photonics*, 2015, **9**, 695-701.
30. Q. Sun, P. Fassi, D. Becker-Koch, A. Bausch, B. Rivkin, S. Bai, P. E. Hopkinson, H. J. Snaith and Y. Vaynzof, *Advanced Energy Materials*, 2017, **7**, 1700977.
31. Z. Guo, Y. Wan, M. Yang, J. Snider, K. Zhu and L. Huang, *Science*, 2017, **356**, 59-62.
32. G. W. P. Adhyaksa, S. Brittman, H. Āboliņš, A. Lof, X. Li, J. D. Keelor, Y. Luo, T. Duevski, R. M. A. Heeren, S. R. Ellis, D. P. Fenning and E. C. Garnett, *Advanced Materials*, 2018, **30**, 1804792.
33. J. M. Snider, Z. Guo, T. Wang, M. Yang, L. Yuan, K. Zhu and L. Huang, *ACS Energy Letters*, 2018, **3**, 1402-1408.
34. S. Nah, B. Spokoyny, C. Stoumpos, C. M. M. Soe, M. Kanatzidis and E. Harel, *Nature Photonics*, 2017, **11**, 285-288.
35. S. Deng, D. D. Blach, L. Jin and L. Huang, *Advanced Energy Materials*, 2020, **10**, 1903781.
36. K. Appavoo, W. Nie, J.-C. Blancon, J. Even, A. D. Mohite and M. Y. Sfeir, *Physical Review B*, 2017, **96**, 195308.
37. T. A. S. Doherty, A. J. Winchester, S. Macpherson, D. N. Johnstone, V. Pareek, E. M. Tennyson, S. Kosar, F. U. Kosasih, M. Anaya, M. Abdi-Jalebi, Z. Andaji-Garmaroudi, E. L. Wong, J. Madéo, Y.-H. Chiang, J.-S. Park, Y.-K. Jung, C. E. Petoukhoff, G. Divitini, M. K. L. Man, C. Ducati, A. Walsh, P. A. Midgley, K. M. Dani and S. D. Stranks, *Nature*, 2020, **580**, 360-366.
38. L. A. Muscarella, E. M. Hutter, S. Sanchez, C. D. Dieleman, T. J. Savenije, A. Hagfeldt, M. Saliba and B. Ehrler, *The Journal of Physical Chemistry Letters*, 2019, **10**, 6010-6018.
39. S. Jariwala, H. Sun, G. W. P. Adhyaksa, A. Lof, L. A. Muscarella, B. Ehrler, E. C. Garnett and D. S. Ginger, *Joule*, 2019, **3**, 3048-3060.
40. T. W. Jones, A. Osherov, M. Alsari, M. Sponseller, B. C. Duck, Y.-K. Jung, C. Settens, F. Niroui, R. Brenes, C. V. Stan, Y. Li, M. Abdi-Jalebi, N. Tamura, J. E. Macdonald, M. Burghammer, R. H. Friend, V. Bulović, A. Walsh, G. J. Wilson, S. Lilliu and S. D. Stranks, *Energy & Environmental Science*, 2019, **12**, 596-606.
41. A. Polman, M. Kociak and F. J. García de Abajo, *Nature Materials*, 2019, **18**, 1158-1171.
42. J. Ran, O. Dycck, X. Wang, B. Yang, D. B. Geohegan and K. Xiao, *Advanced Energy Materials*, 2020, **10**, 1903191.
43. Y. Zhou, H. Sternlicht and N. P. Padture, *Joule*, 2019, **3**, 641-661.
44. H. Sun, G. W. P. Adhyaksa and E. C. Garnett, *Advanced Energy Materials*, 2020, **10**, 2000364.
45. S. Chen and P. Gao, *J. Appl. Phys.*, 2020, **128**, 010901.
46. T. Coenen and N. M. Haegel, *Applied Physics Reviews*, 2017, **4**, 031103.
47. H. Guthrey and J. Moseley, *Advanced Energy Materials*, 2020, **10**, 1903840.
48. D. Cortecchia, K. C. Lew, J.-K. So, A. Bruno and C. Soci, *Chem. Mater.*, 2017, **29**, 10088-10094.
49. W. Li, M. U. Rothmann, A. Liu, Z. Wang, Y. Zhang, A. R. Pascoe, J. Lu, L. Jiang, Y. Chen, F. Huang, Y. Peng, Q. Bao, J. Etheridge, U. Bach and Y.-B. Cheng, *Advanced Energy Materials*, 2017, **7**, 1700946.
50. F. J. Garcia de Abajo, *Rev. Mod. Phys.*, 2010, **82**, 209.
51. J. A. Hachtel, S.-Y. Cho, R. B. Davidson, M. A. Feldman, M. F. Chisholm, R. F. Haglund, J. C. Idrobo, S. T. Pantelides and B. J. Lawrie, *Light: Science & Applications*, 2019, **8**, 33.
52. J. A. Hachtel, R. B. Davidson, E. R. Kovalik, S. T. Retterer, A. R. Lupini, R. F. Haglund, B. J. Lawrie and S. T. Pantelides, *Opt. Lett.*, 2018, **43**, 927-930.
53. S. Yanagimoto, N. Yamamoto, T. Sannomiya and K. Akiba, *Physical Review B*, 2021, **103**, 205418.

54. A. C. Atre, B. J. M. Brenny, T. Coenen, A. García-Etxarri, A. Polman and J. A. Dionne, *Nature Nanotechnology*, 2015, **10**, 429-436.
55. T. Coenen, E. J. R. Vesseur, A. Polman and A. F. Koenderink, *Nano Lett.*, 2011, **11**, 3779-3784.
56. M. A. Feldman, E. F. Dumitrescu, D. Bridges, M. F. Chisholm, R. B. Davidson, P. G. Evans, J. A. Hachtel, A. Hu, R. C. Pooser, R. F. Haglund and B. J. Lawrie, *Physical Review B*, 2018, **97**, 081404.
57. V. Iyer, Y. S. Phang, A. Butler, J. Chen, B. Lerner, C. Argyropoulos, T. Hoang and B. Lawrie, *APL Photonics*, 2021, **6**, 106103.
58. J. T. van Wijngaarden, E. Verhagen, A. Polman, C. E. Ross, H. J. Lezec and H. A. Atwater, *Appl. Phys. Lett.*, 2006, **88**, 221111.
59. M. V. Bashevoy, F. Jonsson, K. F. MacDonald, Y. Chen and N. I. Zheludev, *Opt. Express*, 2007, **15**, 11313-11320.
60. G. Adamo, J. Y. Ou, J. K. So, S. D. Jenkins, F. De Angelis, K. F. MacDonald, E. Di Fabrizio, J. Ruostekoski and N. I. Zheludev, *Phys. Rev. Lett.*, 2012, **109**, 217401.
61. T. Suzuki and N. Yamamoto, *Opt. Express*, 2009, **17**, 23664-23671.
62. K. Takeuchi and N. Yamamoto, *Opt. Express*, 2011, **19**, 12365-12374.
63. X. Ma, M. Grüßer and R. Schuster, *The Journal of Physical Chemistry C*, 2014, **118**, 23247-23255.
64. C. I. Osorio, T. Coenen, B. J. M. Brenny, A. Polman and A. F. Koenderink, *ACS Photonics*, 2016, **3**, 147-154.
65. J. D. Jackson, *Classical Electrodynamics*, 3rd ed., Wiley, 1998.
66. W. Nie, H. Tsai, R. Asadpour, J.-C. Blancon, A. J. Neukirch, G. Gupta, J. J. Crochet, M. Chhowalla, S. Tretiak, M. A. Alam, H.-L. Wang and A. D. Mohite, *Science*, 2015, **347**, 522-525.
67. E. Aydin, M. De Bastiani and S. De Wolf, *Advanced Materials*, 2019, **31**, 1900428.
68. A. Maiti, S. Chatterjee, L. Peedikakkandy and A. J. Pal, *Solar RRL*, 2020, **4**, 2000505.
69. Z. Ni, C. Bao, Y. Liu, Q. Jiang, W.-Q. Wu, S. Chen, X. Dai, B. Chen, B. Hartweg, Z. Yu, Z. Holman and J. Huang, *Science*, 2020, **367**, 1352-1358.
70. V. I. Ethan J. Taylor, Bibek S. Dhami, Clay Klein, Benjamin J. Lawrie, Kannatassen Appavoo, *arXiv:2201.06546*, 2022.
71. O. Hentz, Z. Zhao and S. Gradečak, *Nano Letters*, 2016, **16**, 1485-1490.
72. F. U. Kosasih, S. Cacovich, G. Divitini and C. Ducati, *Small Methods*, 2021, **5**, 2000835.
73. W. Nie, J.-C. Blancon, A. J. Neukirch, K. Appavoo, H. Tsai, M. Chhowalla, M. A. Alam, M. Y. Sfeir, C. Katan, J. Even, S. Tretiak, J. J. Crochet, G. Gupta and A. D. Mohite, *Nat Commun*, 2016, **7**.
74. C. Xiao, Z. Li, H. Guthrey, J. Moseley, Y. Yang, S. Wozny, H. Moutinho, B. To, J. J. Berry, B. Gorman, Y. Yan, K. Zhu and M. Al-Jassim, *The Journal of Physical Chemistry C*, 2015, **119**, 26904-26911.
75. E. F. Schubert, *Light-Emitting Diodes*, Cambridge University Press, 2003.
76. B. J. M. Brenny, T. Coenen and A. Polman, *J. Appl. Phys.*, 2014, **115**, 244307.
77. J.-C. Blancon, W. Nie, A. J. Neukirch, G. Gupta, S. Tretiak, L. Cognet, A. D. Mohite and J. J. Crochet, *Adv. Funct. Mater.*, 2016, **26**, 4283-4292.
78. L. M. Pazos-Outón, M. Szumilo, R. Lamboll, J. M. Richter, M. Crespo-Quesada, M. Abdi-Jalebi, H. J. Beeson, M. Vručinić, M. Alsari, H. J. Snaith, B. Ehrler, R. H. Friend and F. Deschler, *Science*, 2016, **351**, 1430.